Carbon 231 (2025) 119707

Contents lists available at ScienceDirect

Carbon

journal homepage: www.elsevier.com/locate/carbon

Improving photoexcited carrier separation through Z-scheme $W_{18}O_{49}$/BiOBr heterostructure coupling carbon quantum dots for efficient photoelectric response and tetracycline photodegradation

Weiwei Tie [a,b], Surjya Sarathi Bhattacharyya [d], Tianci Ma [a], Shuangyi Yuan [a], Minghan Chen [a], Weiwei He [a,b,**], Seung Hee Lee [c,*]

[a] Key Laboratory of Micro-Nano Materials for Energy Storage and Conversion of Henan Province, Institute of Surface Micro and Nano Materials, College of Chemical and Materials Engineering, Xuchang University, Henan, 461000, PR China
[b] Henan Joint International Research Laboratory of Nanomaterials for Energy and Catalysis, Xuchang University, Xuchang, Henan, 461000, PR China
[c] Department of Polymer Nano-Science and Technology, Department of Nano Convergence Engineering and Department of JBNU-KIST Industry-Academia Convergence Research, Jeonbuk National University, Jeonju, Jeonbuk, 54896, Republic of Korea
[d] Asutosh College, 92 Shyamaprasad Mukherjee Road, Kolkata, West Bengal, 700026, India

ARTICLE INFO

Keywords:
Bismuth oxybromide
Tungsten oxide
Carbon quantum dot
Photoelectric response
Photocatalysis
Tetracycline hydrochloride

ABSTRACT

Building Z-scheme heterostructure integrating oxygen vacancies seems to effectively encourage photoexcited charge partition and hence photoelectric response and photocatalytic performance. Here, through the inclusion of carbon quantum dots (CQDs) with $W_{18}O_{49}$/BiOBr (WB) for enhancing electron exchange and band structure control, we have developed one Z-scheme ternary CQD/$W_{18}O_{49}$/BiOBr heterostructures (CWB) with intense oxygen vacancies. The optimal CWB heterostructure shows superior photocatalytic and photoelectric response execution. The findings indicate that CWB has higher photocatalytic degradation efficiency of tetracycline hydrochloride (TC) at 97 % compared to WB or $W_{18}O_{49}$ alone. Additionally, the CWB shows a higher photocurrent density, surpassing WB and $W_{18}O_{49}$ by 2.5 times and 5.4 times. A potential self-supplied photoelectrochemical-type photodetector utilizing CWB displays relatively quick and stable photoelectric response at 0 V. The improved photo-electric performance are linked to the combined impact of separation and redistribution of charges caused by Z-scheme heterostructure and oxygen vacancies, as well as intensive light absorbance by localized surface plasmon resonance. Our research also validates significance of CQDs as cocatalyst in accelerating the splitting of photo carriers in Z-scheme ternary CWB heterostructures, which will stimulate interest in creating advanced photoactive heterojunction substance with carbon nanomaterials.

1. Introduction

Recent years have seen a substantially increased research interest in the investigation of photoactive semiconducting materials because of their potential applications in hydrogen photo-evolution, water photo-splitting, CO_2 and N_2 photo-reduction, wastewater photo-degradation, and photo-detection [1–7].

Single-phase photoactive systems exhibit significant limitations in practical usage because of their insufficient capacity to harvest light and their inefficiency in the separation, transport, and channelization of photo-excited electron/hole pairs [8–10]. Extensive investigations report that judiciously constructed heterojunctions can solve the mentioned problem in single-phase photoactive systems, and the sunlight absorption range and the efficiency of separation of photoexcited carriers can improve [10–14]. Compared to conventional type-II heterojunctions, Z-scheme heterojunctions have become a research focus due to their strong oxidation and reduction capability and more effective separation of photo-excited carriers than their single-component peers [13–16]. The synergistic effect of Z-scheme heterojunction and localized surface plasmon resonance (LSPR) allows a $W_{18}O_{49}$/BiOBr

* Corresponding author. Department of Polymer Nano-Science and Technology, Department of Nano Convergence Engineering and Department of JBNU-KIST Industry-Academia Convergence Research, Jeonbuk National University, Jeonju, Jeonbuk, 54896, Republic of Korea.
** Corresponding author. Key Laboratory of Micro-Nano Materials for Energy Storage and Conversion of Henan Province, Institute of Surface Micro and Nano Materials, College of Chemical and Materials Engineering, Xuchang University, Henan, 461000, PR China.
E-mail addresses: tieweiwei@xcu.edu.cn (W. Tie), heweiweixcu@gmail.com (W. He), lsh1@jbnu.ac.kr (S.H. Lee).

https://doi.org/10.1016/j.carbon.2024.119707
Received 24 June 2024; Received in revised form 12 September 2024; Accepted 11 October 2024
Available online 12 October 2024

heterojunction to perform better in photocatalytic degradation than its constituent individual molecular components [17] and the SnS_2–$BiVO_4$ Z-scheme heterostructure increases photoelectric response hence, prolonging the lifetime of photo-excited carriers [18].

In recent years, there has been a significant amount of research interest on the metal oxide semiconductor $W_{18}O_{49}$, which appeares favorable over traditional semiconductors like ZnO and TiO_2 because of its ability to absorb solar light over a wide range of frequencies through the LSPR effect, along with numerous surface oxygen vacancies (OVs) [17,19,20]. It is known that these OVs defects alter local atomic coordination environment arround defect sites including coordination number, bond length, and so on; and further tune the carrier dynamics and photocatalytic performance [21,22]. Furthermore, $W_{18}O_{49}$ is known to be a *n*-typed semiconductor with a comparatively small band gap, which has a higher valence band (VB) potential of around +2.76 eV for a high oxidation capacity [22,23]. However, the quick recombination of photo-induced carriers at deep trap states, the lability of surface defects, and its relatively lower conduction band (CB) potential limit the practical application. Hence, in $W_{18}O_{49}$ based Z-scheme photoactive system construction, efficient migrating the electrons from $W_{18}O_{49}$ surface for step photon excitation will be a key to overcome the issues of rapid carrier recombination, unstable surface defects and low conduction band.

Additionally, as a promising *p*-type semiconducting material, layer-structured BiOBr is also of great interest, because of its visible-light-response, superior photocatalytic stability, greater negative CB potential energy, and moderate band gap energy (~2.6 eV) [24–26]. However, the $h_{VB}+$ has to be improved due to its restricted ability to absorb visual light and to oxidize [26,27]. Furthermore, it is discovered that BiOBr's VB and CB positions match $W_{18}O_{49}$'s well [17]. In this way, it can be sensibly anticipated that the Z-scheme heterojunction between *p*-typed BiOBr and *n*-typed $W_{18}O_{49}$ may be accomplished due to their appropriate band structure compatibility, which is expected to be an exceedingly photoactive fabric with self-generated internal electric field (IEF), well-repressed recombination of photogenerated electron-hole sets and relatively fine photo-stability. To further strengthen electron transferring and separation ability, carbon quantum dot (CQD), a quasi-0D carbon nanomaterial with prominent optical execution, prevalent electron exchange, and supply characteristics, nontoxicity, and cheapness, basically composed of sp^2-sp^3 hybridized carbon centers and shells of oxygen-containing species, has been chosen to integrate with BiOBr and $W_{18}O_{49}$ [28,29], to realize the near/close interaction in heterogeneous structures and to reduce charge exchange resistance and quicken the movement of photo-excited carriers owing to their conductivity [30,31]. Besides, CQDs with delocalized π-electrons have moderately low work function (~4.5 eV) compared to most oxide semiconductors (~6 eV in common), which might initiate and upgrade IEF at the heterogeneous interface [30–33]. All the favorable properties recommend CQDs would be a competent electron-cocatalyst and help a photoactive fabric to attain productive charge division and exchange. Subsequently, the development of $W_{18}O_{49}$/BiOBr heterojunction or coupling of CQDs with BiOBr or WO_3 has been well considered to date, which illustrates that the coupling of two distinctive photoactive components may offer predominant light utilization proficiency and quicken charger carrier division [17,30–32]. Be that as it may, this Z-scheme ternary heterostructure of $W_{18}O_{49}$/BiOBr coupling with CQDs counting its effortless union procedure and photoelectric applications counting photoelectrochemical-type (PEC) photodetectors (PD) and tetracycline photodegradation have not been considered however, particularly the commitments of impeded electrons-holes recombination and amplified visible light utilization on the advanced photoelectric division capacity are not clear.

In this paper, we have constructed a ternary Z-scheme heterojunction (CQD/$W_{18}O_{49}$/BiOBr) by basic solvothermal, fluid stage room-temperature response, and ensuing mellow warm treatment preparation, which provides non-expensive-device and facile synthesis convenience. This Z-scheme heterostructure, helped by the CQDs and copious OVs, achieves viable photo-electron-hole partition and appears prevalent photoresponse and photocatalytic debasement of TC poisons outperforming single $W_{18}O_{49}$ or $W_{18}O_{49}$/BiOBr. The CQD/$W_{18}O_{49}$/BiOBr hybrid is utilized as a promising candidate for self-powered PEC PD and ascendant photocatalytic debasement of TC poisons beneath solar illumination. These are credited to the synergistic impact of Z-scheme heterostructure and OVs, together with intensive light absorbance by LSPR, inducing proficient charge division, favorable h^+、$\cdot O_2^-$ and ·OH generation. The development of OV-rich and conductive 0D/1D/2D ternary heterostructures might bring unexplored openings for the sound plan of exceedingly photoactive materials for natural remediation and low-energy photo-detection applications.

2. Experimental

2.1. Materials

The reagents and materials utilized here are all analytical grade and used as received without additional purification. Bismuth(III) nitrate pentahydrate ($Bi(NO_3)_3{\cdot}5H_2O$), Citric acid monohydrate (CA), Hexadecyltrimethylammonium bromide (CTAB), Ethylenediamine, Tungsten hexachloride (WCl_6), 1,4-benzoquinone (BQ), Ethylenediaminetetraacetic acid disodium salt dihydrate (EDTA-Na_2), Isopropanol (IPA), absolute ethanol, n-octane and Tetracycline hydrochloride ($C_{22}H_{24}N_2O_8{\cdot}HCl$, TC) are supplied by Shanghai Aladdin biochemical Polytron Technology Co. Besides, other commercially chemical reagents used are purchased from the Sinopharm Chemical Reagent Plant (China).

2.2. Preparation of CQD

The CQDs are synthesized using a modified one-step hydrothermal method as described previously [29]: 3 g of CA is dissolved in 10 mL of deionized water in a Teflon-lined autoclave. Subsequently, 0.8 mL of ethylenediamine is added. After dispersing, the above mixture is heated to 190 °C for reaction 8 h. Until cooling, the resulting dark-brown solution undergoes dialysis for 24 h to obtain the dialyzed CQD solution with concentration of about 1.3 mg/mL, and finally, dry CQDs are obtained by lyophilizing process.

2.3. Preparation of $W_{18}O_{49}$

The $W_{18}O_{49}$ nanowires are synthesized through a modified solvothermal method using WCl_6 as a precursor [20]. The process is as follows: 0.1 g of WCl_6 is added into 30 mL anhydrous ethanol in a Teflon-lined autoclave, after fully stirring and dissolving, the reaction occurs at 200 °C for 6 h. After the reaction, the mixture is centrifuged together with washing, and drying in a vacuum oven to obtain $W_{18}O_{49}$.

2.4. Preparation of $W_{18}O_{49}$/BiOBr

The $W_{18}O_{49}$/BiOBr composite is obtained in n-octane/water system via a room temperature method with modifications [27]: 0.25 g of $W_{18}O_{49}$ is dispersed in 12.5 mL n-octane containing 0.364 g of CTAB; meanwhile, 0.485 g of $Bi(NO_3)_3{\cdot}5H_2O$ and 0.072 g of CA slowly are added into 7.5 mL deionized water with sufficient stirring, respectively; afterwards, this aqueous solution slowly drops into the above organic solution and react under intense stirring for 30 min; Finally, the as-prepared $W_{18}O_{49}$/BiOBr is received after alternate centrifuging/washing for several times and vacuum drying at 60 °C. As a comparison, pure BiOBr is synthesized without adding of $W_{18}O_{49}$ according to similar procedures.

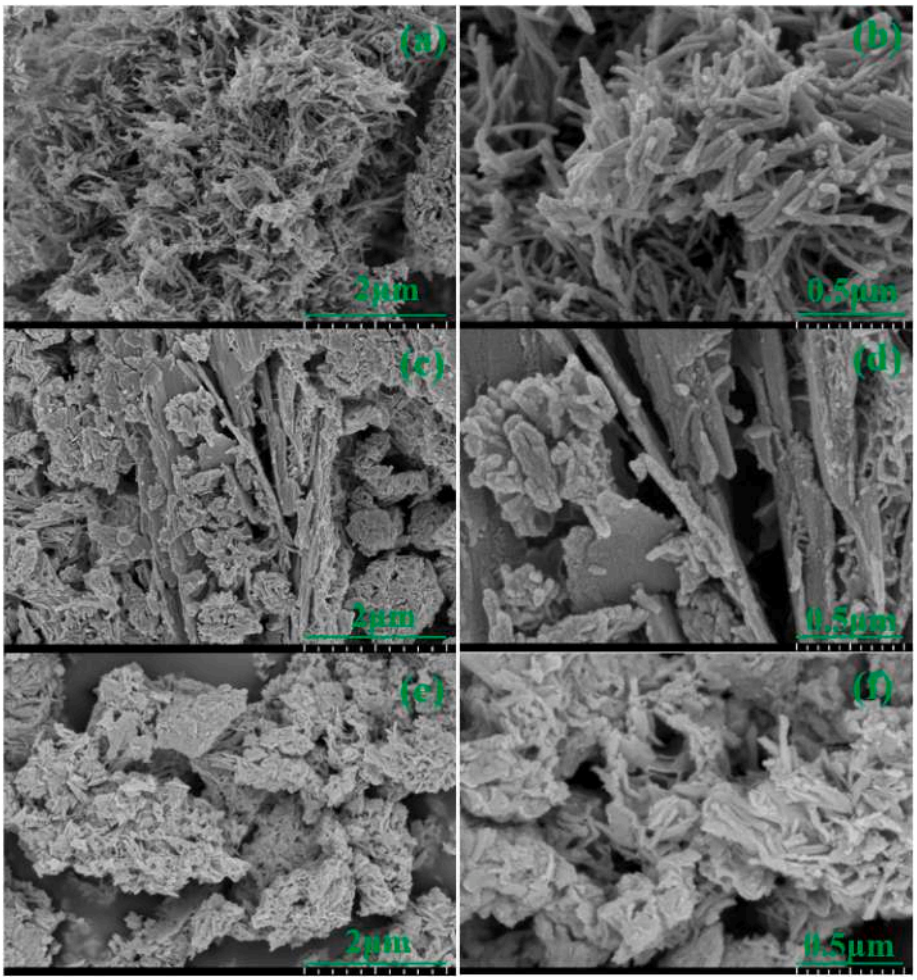

Fig. 1. SEM images of prepared samples ($W_{18}O_{49}$ (a,b); WB (c,d); CWB-2 (e,f)).

2.5. Preparation of CQD/$W_{18}O_{49}$/BiOBr

50 mg of the above prepared $W_{18}O_{49}$/BiOBr is dispersed in certain amount of CQD aqueous solution under 10 min ultrasonic action and constantly stirring for 3 h, and then the mixture is heated at 70 °C for 8 h in an oven until the liquid evaporation completes; Afterwards, CQD/$W_{18}O_{49}$/BiOBr samples are obtained after centrifuging, washing and vacuum drying at 60 °C. According to the mass content of CQDs used, samples have been named as CWB-1, CWB-2, CWB-3, CWB-4 (CWB-1: 12 wt%, CWB-2: 21 wt%, CWB-3: 25 wt%; CWB-4: 28 %).

2.6. Characterization

Microscopic morphology and microstructures as well as elemental compositional analysis of prepared samples are performed using a field emission scanning electron microscope with energy-dispersive X-ray (EDX) spectrometer (SEM, SU8010, HITACHI; EMAX mics 2, HORIBA) and field emission transmission electron microscope (TEM, FEI Tecnai G2/F30; FEI Tal os F200X). The crystal structures are determined by a X-ray diffractometer (XRD, Bruker D8/Advance, Germany) with Cu-Kα radiation (λ = 1.5406A°). The functional structure of as-produced samples is identified by Fourier transform infrared spectroscopy (FTIR, Nicolet 6700). The chemical state and composition of series of samples is performed using X-ray photoelectron spectroscopy (XPS, Thermo escalab 250Xi). The specific surface area and pore diameter are recorded and evaluated by measuring N_2 adsorption/desorption isotherms on a surface area using porosimetry analyzer (Micromeritics, ASAP2460). The optical absorption characteristic of series of samples is evaluated through UV/vis diffuse reflectance spectra (DRS, Cary 5000, Agilent, USA) while $BaSO_4$ is used as a reference sample. The radicals occurred in prepared samples are investigated on electron spin resonance spectrometer (ESR, Bruker A300-10/12, Germany).

2.7. Photocatalytic activity measurements

Photo-catalytic activity tests of tetracycline hydrochloride (TC) with obtained samples are performed in a reaction beaker equipped with a circulating water device under a 300 W Xenon lamp (PLS-SXE300/300UV) with irradiation power of arround 300 mW/cm^2. The specific process is as follows: 20 mg of each sample is dispersed in TC aqueous solution (20 mg/L, 50 mL) following the adsorption/desorption equilibrium process under dark conditions [22]. Then, each sample supernatant is taken when the light turns on at intervals and centrifuged to remove photoactive materials. Next, the absorption intensity of the solution at the maximum absorption wavelength (356 nm) at different times is recorded by UV-vis spectroscopy (Cary 5000, Agilent, USA). By comparing, the photo-catalytic activity of each material is evaluated by the following formula (1) [12,13].

$$R = C_t/C_0 \quad (1)$$

Where: R is photo-catalytic activity (%); C_0 and C_t are the original absorption of TC in aqueous solution at different dark and light time T, respectively.

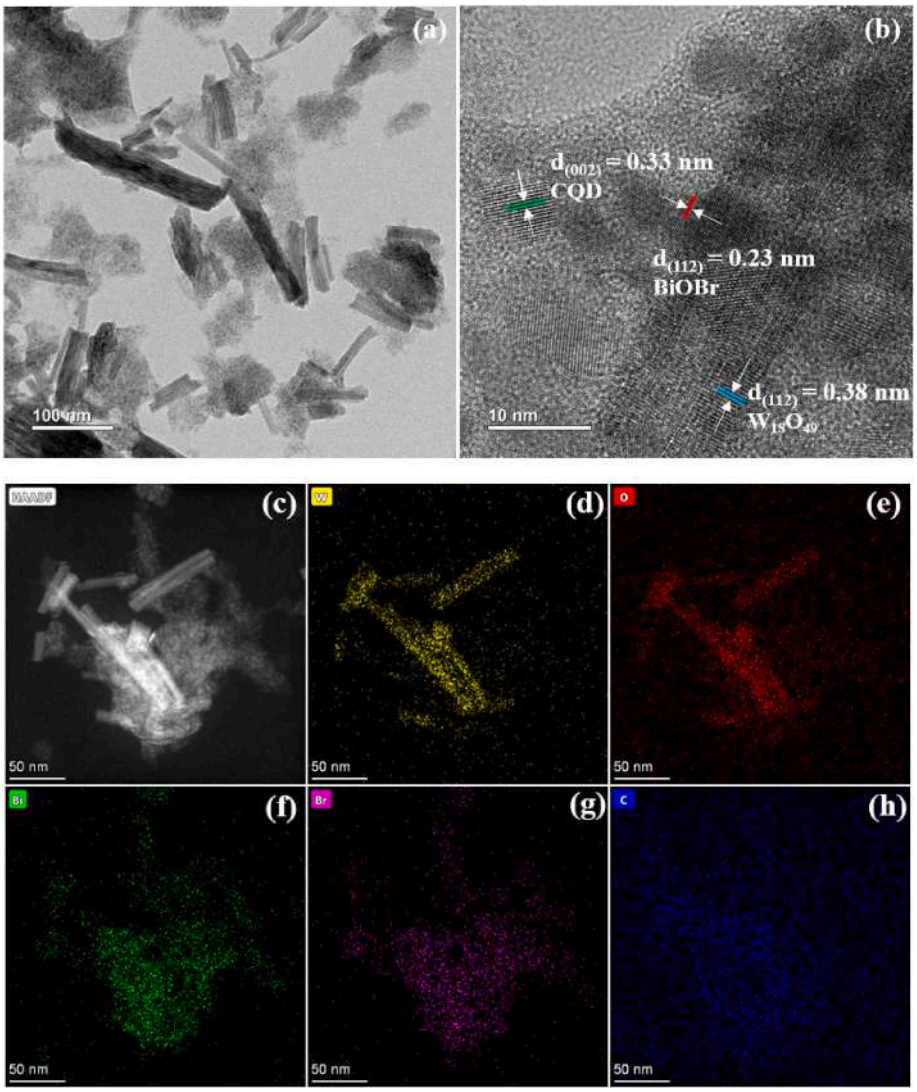

Fig. 2. TEM (a), HRTEM (b), HAADF-STEM (c) of CWB-2 sample and corresponding elemental mapping: (d) W; (e) O; (f) Bi; (g) Br; (h)C.

2.8. Photoelectrochemical measurements

Photo-electrochemical measurements are carried out through CHI 660E electrochemical workstation with a standard three-electrode system [6]: reference electrode-Ag/AgCl; counter electrode-platinum sheet; working electrode-indium-tin oxide sheet glass (ITO) coated with different prepared photoactive samples: 5 mg of each sample is weighed and mixed well with 1 mL of NMP, and then, the mixture is coated on ITO glass with a effective coating/measuring area of 1 cm^2 until dry in vacuum and take out for use. Light irradiation intensity of 100 mW cm^{-2} (I) is provided and all photo-electrochemical tests are studied at room temperature in electrolyte of 0.5 M Na_2SO_4 solution with volatge applied ranging from 0 V to 1 V (vs. Ag/AgCl) with certain time interval.

3. Result and discussion

Morphological features of as-produced samples are observed by SEM and TEM as presented in Figs. 1 and 2. It can be seen from Fig. 1 (a, b) that $W_{18}O_{49}$ as a whole displays a one-dimensional (1D) nanowire shape. In Fig. 1(c, d), $W_{18}O_{49}$/BiOBr (WB) thus exhibits a nanowire/flake stacking state with irregular pores, suggesting that $W_{18}O_{49}$ and BiOBr are successfully held together. Besides, porous stacking morphologies are also observed in CQD/$W_{18}O_{49}$/BiOBr (CWB-2) in Fig. 1(e, f). Notably, no observation of CQDs with particle size less than 10 nm may be due to the limited resolution of SEM. Besides, the employed energy-dispersed X-ray results (EDX) of WB and CWB-2 has been listed in Table 1S. Both WB and CWB-2 consist of W, O, Bi, Br, and C, which, to a certain extent, shows the compositional changes before and after CQD introduction. To further explore morphological characteristics of CQD/$W_{18}O_{49}$/BiOBr, TEM measurement has been carried out and presented in Fig. 2 and Fig. S1. Clearly, CWB-2 displays self-assembled morphology and black CQD assembled with sheet-like BiOBr and $W_{18}O_{49}$ nanowires could be found in Fig. 2a,b, in which 1D $W_{18}O_{49}$ exhibits diameters in range of about 7–45 nm; BiOBr are composed of 2D flake with sizes around 40–245 nm, and obtained CQD particles with sizes of about 4–8 nm decorated over $W_{18}O_{49}$/BiOBr heterostructure, which display similar sizes compared to single component (Fig. S1); Besides, the optical absorption property of CQD is consistent to the reported literature shown in Fig. S2 [29]; and the lattice spacing of 0.33 nm, 0.23 nm, 0.38 nm could be observed in and indexed to (002), (112), (010) facets of CQD, BiOBr, and $W_{18}O_{49}$, respectively [30,34,35]. Subsequently, the chemical composition and spatial distribution of the CWB-2 have been employed using the HAADF-STEM and corresponding elemental mapping as shown in Fig. 2(c–h). The results indicate that the CWB-2 consists of W, O, Bi, Br, and C, confirming the coexistence of CQD, $W_{18}O_{49}$, and BiOBr. The above results demonstrate the excellent combination of abovementioned triple components in CWB, possessing clear crystal stripes, intertwined, and tightly bounded interfaces.

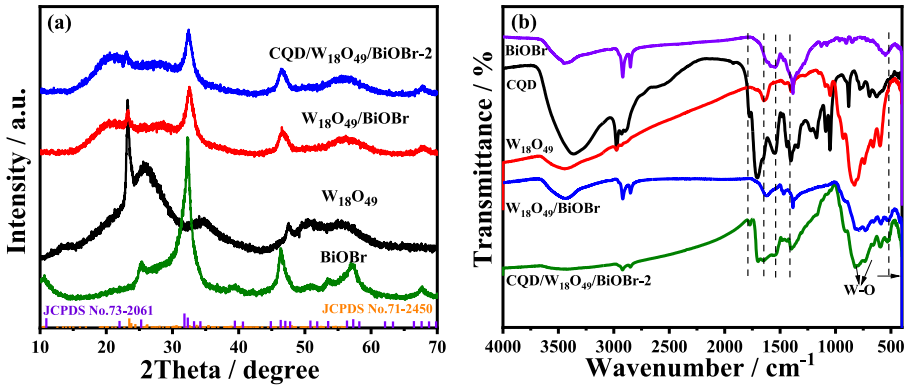

Fig. 3. XRD pattern(a) and FT-IR spectra (b) of the series of samples.

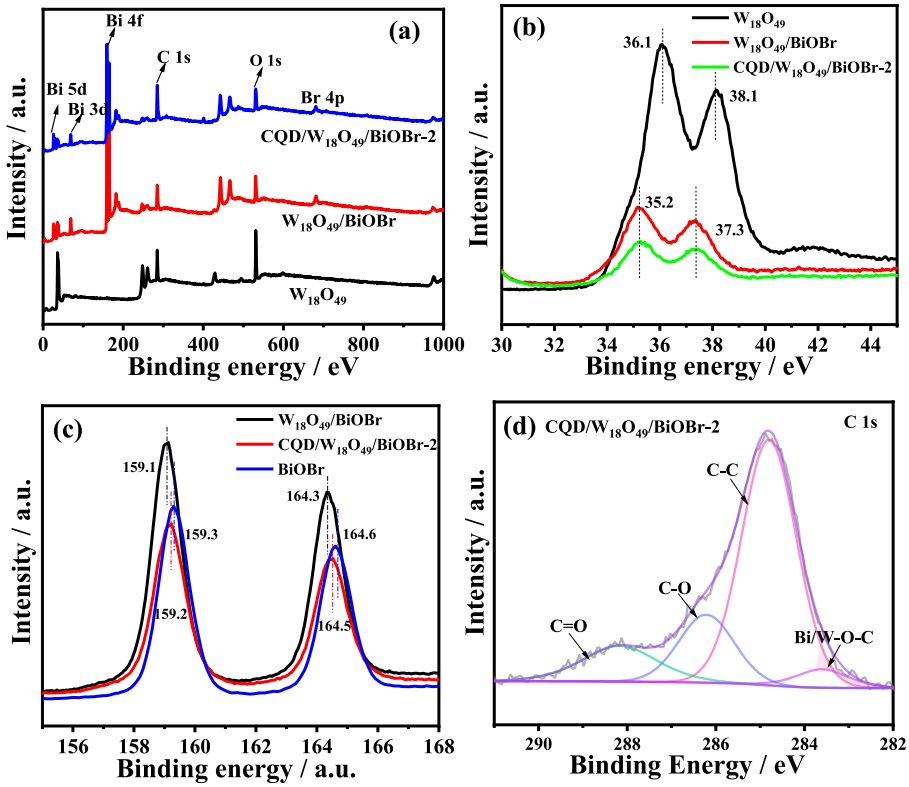

Fig. 4. XPS spectra of series of samples. (a) survey spectra, (b) W 4f core level, (c) Bi 3d core level, (d) C 1s core level.

The crystal structure of as-prepared materials is recognized by XRD investigation, and the results are shown in Fig. 3a. It can be observed that the diffraction peaks in pure $W_{18}O_{49}$ mainly appear at 23.2° and 47.5° respectively, which corresponds to the (010) and (020) crystal faces of $W_{18}O_{49}$ (JCPDS No.71-2450) [19,35], and no impurity peaks are observed, indicating that prepared $W_{18}O_{49}$ has high purity. For BiOBr, the diffraction peaks appear at 10.5, 25.3, 32.3, 39.5, 46.5, 50.7, 57.3, 66.7°, corresponding to the crystal faces of (001), (011), (110), (112), (020), (014), (212), and (220), respectively, (JCPDS No.73-2061) [31,36]; Meanwhile, the (010) facet of $W_{18}O_{49}$ and (110) facet of BiOBr can also be observed in the XRD patterns of $W_{18}O_{49}$/BiOBr and CWB-2, indicating that successful synthesis of $W_{18}O_{49}$/BiOBr heterostructure. In addition, after the combination of CQD onto $W_{18}O_{49}$/BiOBr, the XRD pattern of CWB-2 not only displays characteristic diffraction peaks corresponding to $W_{18}O_{49}$ and BiOBr, but a wide characteristic peak likely belonging to the (002) crystal face of CQD also appear around 21°, which is consistent with literature reports [29]. The results show that CQD, $W_{18}O_{49}$, and BiOBr are assembled. Subsequently, this multi-component sample has been further characterized in the following sections.

Furthermore, the chemical bonds and functional groups of the series of samples have been carried out through FT-IR analysis and depicted in Fig. 3b. Characteristic peaks in pure $W_{18}O_{49}$ and BiOBr appear 630-820 cm^{-1} and around 546 cm^{-1}, attributing to the stretching vibration of W–O and Bi–O bond of tungsten oxide and BiOBr [30,31]. For $W_{18}O_{49}$/BiOBr and CWB-2, W–O (630-820 cm^{-1}), Bi–O (524 cm^{-1}) stretching vibration peaks all occur, indicating that $W_{18}O_{49}$ and BiOBr are successfully combined together, but the Bi–O bands in $W_{18}O_{49}$/BiOBr and CWB-2 all have wavenumber shifts from 546 $cm^{-1}$to 524 cm^{-1} compared to pure BiOBr, indicating the existence of the interaction between $W_{18}O_{49}$ and BiOBr [30,31,33]. Meanwhile, pure CQDs display rich functional groups and chemical bonds, where the stretching vibration peaks are observed at 1547 cm^{-1}, 3400 cm^{-1}, 1396 cm^{-1}, and 1062 cm^{-1}, 1780-1610 cm^{-1}, correspond to the –NH, –OH,

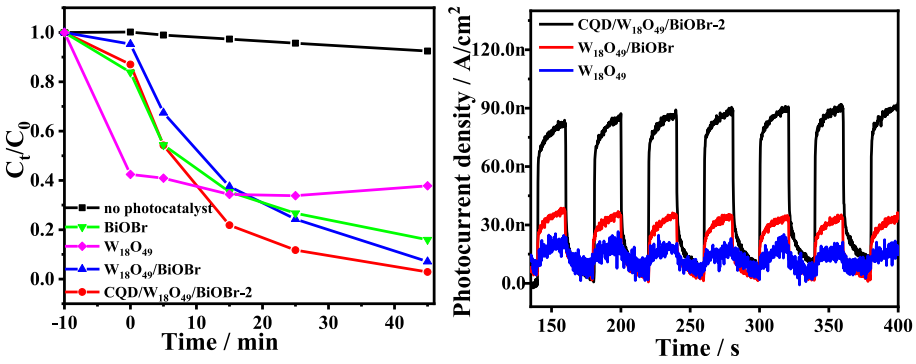

Fig. 5. Photocatalytic activity (a) of series of samples onto TC under sunlight irradiation, and transient photocurrent response (b) of series of samples.

–CN, and oxidative functional groups (C–O–C; carbonyl), respectively [13,30,33]. Moreover, the stretching vibration peaks of –NH, –CN, carbonyl functional groups attributed to CQD also appear in CWB-2, indicating that facile fabrication has successfully loaded CQD onto $W_{18}O_{49}$/BiOBr [13,30,31,33], which is consistent with XRD and TEM analysis. The FT-IR results incorporation with above mentioned other measurements indicates the successful construction of $W_{18}O_{49}$/BiOBr heterostructure and introduction of CQD to a certain extent.

Fig. 4 delineates the XPS investigation of series of samples' chemical composition and their characteristic XPS peak position, inferring for bonding presence in heterostructures from their shifting. The XPS survey spectra of CWB-2 confirms the coexistence of Br, Bi, O, C, and W components (Fig. 4a). Other than that, the high-resolution XPS spectra of the mentioned elements appear in Fig. 4b-d. The W4f center level range of $W_{18}O_{49}$ shows up at 36.1 and 38.1 eV due to $W4f_{7/2}$ and $W4f_{5/2}$ [17]. Particularly, binding energies of $W4f_{7/2}$ and $W4f_{5/2}$ for $W_{18}O_{49}$/BiOBr and CWB-2 move to lower vitality esteem when compared to immaculate $W_{18}O_{49}$, this obvious shift of W peak positions demonstrates the extra inclination of electron exchange due to probable formation of chemical bond at the interface of $W_{18}O_{49}$ and BiOBr (Bi–W) [32,36,37]; However, there is no obvious peak position shift after $W_{18}O_{49}$/BiOBr coupling with CQD [36,37]. Moreover, Bi 4f (Fig. 4c), is derived from BiOBr, and allocated to the chemical state Bi^{3+} [13,33], because it exhibits normal bimodal crests at 164.6 eV (Bi $4f_{5/2}$) and 159.3 eV (Bi $4f_{7/2}$); When $W_{18}O_{49}$/BiOBr is formed, the binding energy of Bi $2f_{5/2}$ and Bi $2f_{7/2}$ for $W_{18}O_{49}$/BiOBr moves to 164.3 eV (Bi $4f_{5/2}$) and 159.1 eV (Bi $4f_{7/2}$); after CQD coupling onto $W_{18}O_{49}$/BiOBr, the binding energy of Bi $2f_{5/2}$ and Bi $2f_{7/2}$ for CWB-2 also moved toward the higher energy level at 164.5 eV (Bi $4f_{5/2}$) and 159.3 eV (Bi $4f_{7/2}$), which probably shows that comparable charge exchange may happen from BiOBr to CQD due to the likely presence of certain chemical bond induced robust interaction between CQD and BiOBr. Similar results are obtained when C materials modify BiOBr or ZnO [14,36,37]. In conclusion, the binding energy shifting can be attributed to the variation of the interfacial chemical environment resulting from the interaction between $W_{18}O_{49}$, CQD, and BiOBr.

For further analysis, the high-resolution C 1s core level spectra of CWB-2 are analyzed with peak differentiating and fitting (Fig. 4d). The main peak of CWB-2 can be fitted into four gaussian peaks, and; the fitted four peaks corresponding to the typical functional groups can be assigned to C–C (284.8 eV), C–O (286.2 eV), C═O (288.2 eV), and C–O–W/Bi (283.6 eV) bonds, respectively [33,38]. To sum up, it is evident that the formation of the C–O–W/Bi bond is obtained in CWB-2 after CQD further coupling with $W_{18}O_{49}$/BiOBr. Therefore, we believe that a good contact exists between $W_{18}O_{49}$, CQD, and BiOBr, rather than a simple physical connection, and this stable interaction and transfer of photo-produced electrons between each component in CWB is shaped through the interfacial chemical interaction as proposed by the mentioned results [14,33,36–38].

We have carried out photo-degradation tests of tetracycline hydrochloride (TC) aqueous solution with a series of samples beneath sunlight stimulation and evaluated their photo-catalytic activity (Fig. 5a). This, to a certain extent, indirectly reflects the photoexcited carrier separation behavior. The expulsion of TC without the catalys's help is less than 10 %, showing that TC has prolonged chemical stability in the aqua environment. $W_{18}O_{49}$ accomplishs about 62.2 % TC debasement, which has elevated light absorption and highly positive VB potential proved by subsequent tests. Be that as it may, photocatalytic debasement might not be realized due to its quick recombination rate of photogenerated electron-hole sets. The other BiOBr alone shows ~84.4 % TC degradation efficiency, which is a much higher photocatalytic action than $W_{18}O_{49}$. After heterojuction establishement, $W_{18}O_{49}$/BiOBr composite efficiently improves TC degradation efficiency to ~92.9 % and, such improvement might have been caused by the impact of proficient electron exchange between $W_{18}O_{49}$ and BiOBr. In addition, the degradation efficiency utilizing CWB-2 has also been expanded further to 97.3 % after introducing CQD, indicating that the improvement of photoexcited carrier separation. Meanwhile, the optimal mass content of CQD used in series of CWB samples have been investigated through photodegrading process of TC, shown in Fig. S3. CWB-2 displays optimal photocatalytic profermance among series of CWB samples with different mass content of CQD used. For further study, the TC photo-degradation process is explored by applying a pseudo-first-order reaction [27,39]. The calculated kinetic rate constant (k) of CWB-2 sample is 0.075 min^{-1}, and is almost 1.3 times higher than that of WB sample; and which is approximately 2.2 and 26.7 times higher than those obtained for BiOBr and $W_{18}O_{49}$, respectively (Fig. S4). The photocatalytic rates continuely increase after Z-scheme heterojuction construction as well as intergating with CQD. Therefore, the photocatalytic degradation rate of TC by different materials from lower to higher value can be arranged in the following order $W_{18}O_{49}$<BiOBr < WB < CWB-2. These outcomes indicates both Z-scheme heterostructure development and CQD adjustment are successful ways to move forward the photocatalytic movement, showing that the CWB composite is a good photoactive fabric. Table 2S displays the photodegradation results of series of Z-scheme heterojunctions in other reported works onto TC [17,31,39–44]. We can see that optimal CWB, in our work, displays comparable photocatalytic degradation ability for TC, from which it should be believed that as-prepared CWB shows certain potential for treating TC.

For the differentiation of photoinduced carrier separation and migration behavior of these photoactive materials, the transient photocurrent response is further investigated by an electrochemical workstation with the standard three-electrode system, following above photoelectrochemical measurements described [8]. Fig. 5b shows the corresponding photocurrent density-time curves at 0.4 V. Pure $W_{18}O_{49}$ shows poor light response with a photocurrent density (J_{ph}, $J_{ph} = J_i - J_d$, where J_i and J_d are the photocurrent density with or without irradiation, respectively) of 15.2 nA cm^{-2} [45,46]. $W_{18}O_{49}$/BiOBr possesses strong photoresponse with a high J_{ph} of 32.7 nA cm^{-2}, additionally, and $W_{18}O_{49}$/BiOBr after integrating with CQD displays higher

Table 1
BET surface area, pore size, and pore volume for series of samples.

Samples	BET surface area (m^2/g)	Pore Size (nm)	Pore Volume(cm^3/g)
$W_{18}O_{49}$	64.6348	13.8774	0.210125
BiOBr	7.2714	26.3158	0.053168
$W_{18}O_{49}$/BiOBr	21.9120	22.0437	0.121805
CQD/$W_{18}O_{49}$/BiOBr-2	21.7189	22.5373	0.122154

photoresponse with a high J_{ph} of 81.4 nA cm^{-2}, which is significantly superior to $W_{18}O_{49}$ and $W_{18}O_{49}$/BiOBr (about 5.4 and 2.5 times). Here, anodic photocurrents for all samples appear at 0.4 V, and the photoelectrodes (working electrode) function as anode. An increase in photocurrent intensity directly indicates a boosted capability for electron generation as well as charge sepatation and transfer to the surface. Combined with the remarkable photoresponse enhancement, it is verified that $W_{18}O_{49}$/BiOBr heterojunction construction and further coupling with CQD all accelerate exciton dissociation into photogenerated carriers and inhibit the e^--h^+ recombination.

The BET surface area and porosity of $W_{18}O_{49}$, BiOBr, WB, and CWB-2 are investigated by N_2 adsorption-desorption measurement for evaluating the role of adsorption in photocatalytic performance, as shown in Fig. S5, and the measured BET surface area, pore size, and pore volume for series of samples are listed in Table 1. Usually, the BET surface area is related to the catalysts' active sites and it is generablly recognized that large BET surface area is conductive to produce high photocatalytic activity [40]. However, it is found that the BET surface areas of WB and CWB-2 lie between $W_{18}O_{49}$ and BiOBr, which are highest and lowest; and pore sizes of WB and CWB-2 are also moderate compared to individual $W_{18}O_{49}$ and BiOBr. However, this is not consistent with the above-mentioned photocatalytic degradation rate order of TC, which indicate that photocatalytic activity of WB and CWB-2 are higher in comparison with individual $W_{18}O_{49}$ and BiOBr, but their BET surface areas (pore sizes) are moderate in series of samples. So, moderate BET

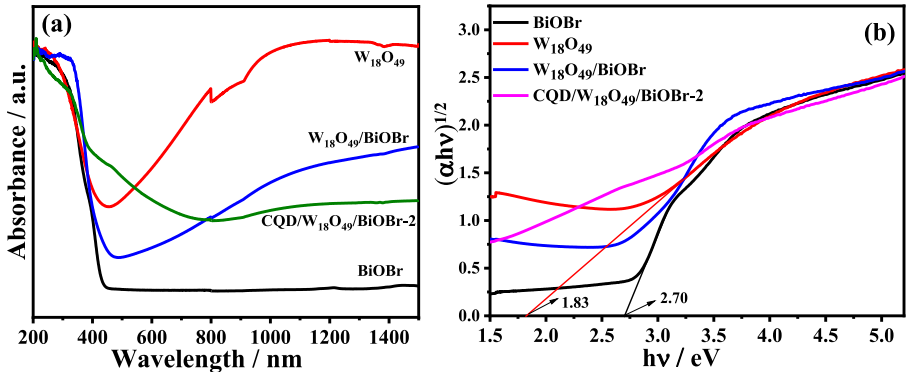

Fig. 6. Diffuse reflectance absorption spectra (a) and Tauc plots showing the band gap (b).

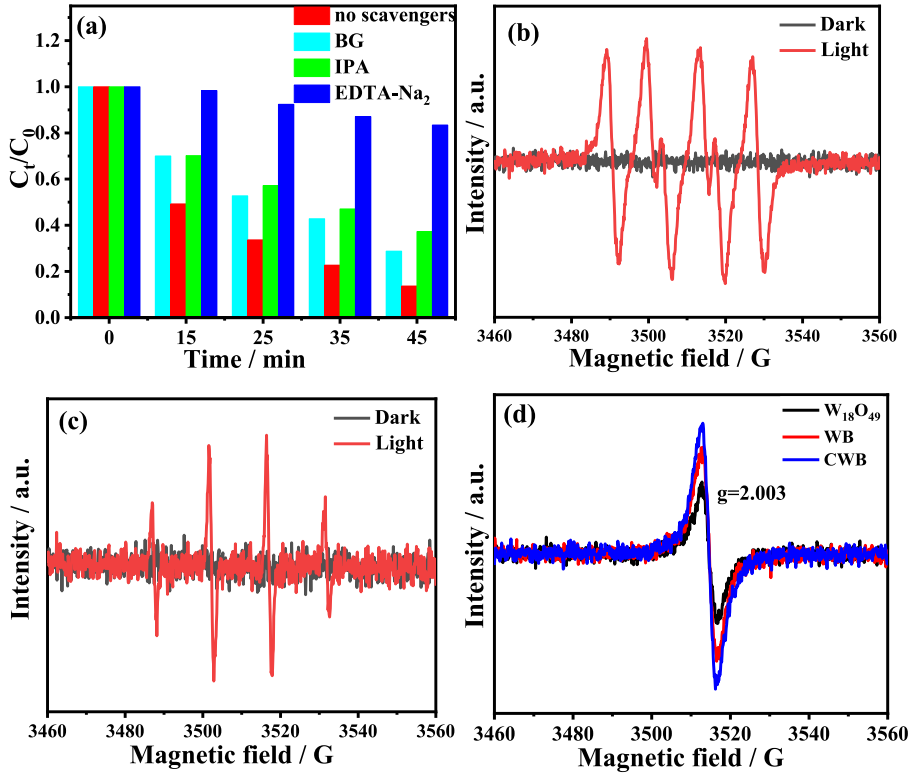

Fig. 7. Photodegradation dynamics (a) of TC in the presence of CWB-2 with and without addition of different scavengers, and ESR spectra of CWB-2 (b–d).

surface areas indicate that BET is not mainly responsible to the enhancement of TC photo degradation profermance in our system [40,47].

The light absorption characteristic of series of photoactive samples is performed through UV–vis diffuse reflectance spectra (DRS) to explore the factors affecting the photo-electric profermance difference as shown in Fig. 6a. Pure BiOBr displays a substantial reaction in UV–visible-light frequencies, but the assimilation edge remains unchanged at approximately 430 nm. By contrast, unadulterated $W_{18}O_{49}$ displays a UV–vis and near-infrared light (NIR) assimilation capacity, credited to the arrangement of surface OVs actuated LSPR effect [17,20,22]. Concurring with the literature, the essential part of OVs in $W_{18}O_{49}$ is to realize Vis-NIR assimilation and production of high-energy hot electrons through the LSPR excitation-induced near-field upgrade impact [17,20,22]. Combining BiOBr with $W_{18}O_{49}$, particularly after introducing CQD, the visible and near-infrared light absorption operation of $W_{18}O_{49}$/BiOBr and CWB-2 has been upgraded compared to immaculate BiOBr attributed to LSPR impact of $W_{18}O_{49}$, which is advantageous for advancing photoresponse and photocatalytic execution. The recorded absorption intensity in CWB-2 is significantly enhanced than that of $W_{18}O_{49}$/BiOBr and immaculate BiOBr within the wavelength range of 400–800 nm credited to fabulous up-conversion fluorescence execution of CQDs [13,33]. In this way, the superior light absorbance execution of CWB forecasts the synergistic impact of the delivered O vacancies in $W_{18}O_{49}$, and fabulous up-conversion fluorescence execution of CQDs as well as enhanced interaction between diverse components of $W_{18}O_{49}$, BiOBr, and CQD. The band gap energies (E_g) of a series of samples are calculated by empirical equation $(\alpha h\upsilon)^{1/2} = A(h\upsilon\text{-}E_g)$, among them, the parameter α, hυ, E_g and A represents absorption coefficient, photo energy, band gap energy, and a constant, respectively [27,36]. According to the calculation (Fig. 6b), the band gaps (E_g) of BiOBr and $W_{18}O_{49}$, are evaluated as 2.70 eV and 1.83 eV, respectively.

We have investigated photo-generated free radicals trapping experiments to affirm their contribution in the photodegradation of TC with CWB-2. Fig. 7a exhibits that the additives viz. 1,4-benzoquinone (BQ, as $\cdot O_2^-$ forager), isopropanol (IPA, as ·OH forager), and ethylenediaminetetraacetic acid disodium salt (EDTA-Na_2, as hole scavenger) all diminishes the debasement rate of TC, illustrating that the photogenerated holes, ·OH and $\cdot O_2^-$ radicals all take part within the TC degradation but with diverse commitment [13,30,33,38]. The existence of $\cdot O_2^-$ and ·OH scavengers diminishes the degradation rate to 71.3 % and 62.8 %, be that as it may, supplementation of EDTA-Na_2 significantly hinders the degradation rate to roughly 16.6 %, which uncovers that the h^+ plays the critical part in degradation process. Summing up, within the photocatalytic degradation of TC by CWB-2, $\cdot O_2^-$, ·OH, and h^+ dynamic species all have unequivocal catalytic corruption impacts on TC, but h^+ plays a vital part within the debasement of TC; because it can also change over to other active substances (i.e., ·OH and H_2O_2) to indirectly debase organic substances.

Numerous studies with Z-scheme heterojunction system on TC intermediates and possible degradation pathways have already been done [41,44,48]. It is reported that TC molecules contain double bonds, amine and phenolic groups, displaying high electron density, which are easy to be attacked by active species (ROS: $\cdot O_2^-$, h^+, ·OH). When the active free radicals of $\cdot O_2^-$, h^+, ·OH all participate in TC photo-degradation process, TC may be degraded due to the shedding of different functional groups through undergoing several major pathways (removal of amide group, dimethylamine, as well as dehydroxylation, ring opening, deethylation and dehydrogenation), and finally broken down into small molecules or ions, which are much similar to our system [44,48]. Therefore, similar intermediates may genergate in similar degradation processes with Z-scheme multicomponent system.

To further illustration of the component for the photocatalytic debasement of TC, the ESR method is utilized to affirm the existence of ·OH and $\cdot O_2^-$ radicals shown in Fig. 7 [35,39,48]. Nearly no characteristic crests are observed, but six DMPO-·O_2^- characteristic signal crests

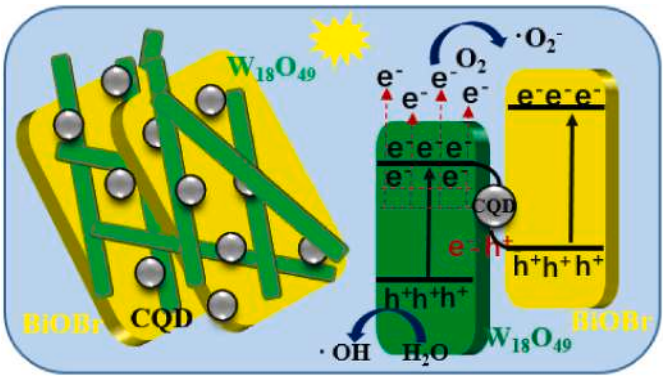

Fig. 8. Possible Z-scheme electron transfer mechanism in CQD/BiOBr/$W_{18}O_{49}$ under light irradiation.

and four DMPO-·OH characteristic crests can be watched beneath light as appeared in Fig. 7b and Fig. 7c. Hence, the ESR results straightforwardly demonstrate existence of $\cdot O_2^-$ and ·OH radicals within CWB-2, which agrees with the radical extinguishing tests. The radical examinations and ESR investigation illustrate that the $\cdot O_2^-$, h^+, and ·OH species play a role within the photocatalytic oxidation of TC. In addition, the ESR measurement is also carried out to provide fingerprint evidence for probing oxygen vacancies (O Vs). As shown in Fig. 7d, a sharp signal at g = 2.003, which is identified as the electrons trapped on O Vs [17,49,50], is detected in pure $W_{18}O_{49}$, WB and CWB-2 sample, verifying again that the OVs exist in the as-prepared samples. Even more remarkably, this signal strength distinctly increases in WB, especially in CWB-2. Due to ESR characterization, we can confirm that the concentration of O Vs in CWB-2 is richest, while that is poor in pure $W_{18}O_{49}$. Larger number of O Vs associated with good contact between multi-components, confirmed by TEM and XPS analysis, will assist in promoting separation and transfer of photoexcited carriers in WB and CWB-2, indicating that it is conducive to improving photoresponse and photocatalytic performance.

For confirming the CWB' charge separation process, the energy band structure is explored by above mentioned XPS valence spectra and UV–vis DRS analysis. The valence band (E_{VB}) top can be investigated by XPS valence band spectra (Fig. S6). The valence band (E_{VB}) maximum energies of pure BiOBr and pure $W_{18}O_{49}$ are 2.27 eV and 2.52 eV, respectively. According to the energy band structure formula $E_{CB} = E_{VB} - E_g$, the conduction band (E_{CB}) of BiOBr and $W_{18}O_{49}$ are calculated to be −0.43 eV and +0.69 eV, respectively [27,33]. In terms of the above description, the VB potentials of BiOBr and $W_{18}O_{49}$ are +2.27 and + 2.52 eV and the CB potentials of BiOBr and $W_{18}O_{49}$ are −0.43 eV and +0.69 eV, individually. The position of CB for $W_{18}O_{49}$ is lower than BiOBr and the position of VB for BiOBr is higher than that of $W_{18}O_{49}$. Fig. 8 depicts a potential Z-scheme charge transfer mechanism. Beneath light illumination, both $W_{18}O_{49}$ and BiOBr in CQD/$W_{18}O_{49}$/BiOBr can be energized to create photo-induced electrons and holes. Then, the CQDs, act as the most important accelerating and the exchange agents of electrons [13,33], promotes the recombination of the VB holes of BiOBr with the CB electrons of $W_{18}O_{49}$ to attain the Z-scheme heterojunction. Subsequently, the e^- on the CB of BiOBr and the h^+ on the VB of $W_{18}O_{49}$ may keep up solid oxidation reducibility and at long last, O_2 within the watery environment chemically reacts with e^- on the CB of BiOBr to make $\cdot O_2^-$, and encourage oxidize poison TC to be debased; on the other hand, h^+ on the VB of $W_{18}O_{49}$ would straightforwardly mineralize TC or chemically react with H_2O to create ·OH to expel TC [13,17,33]. Additionally, O Vs might act as an inter-valence band that worked as an opening for photogenerated e^- transitory accumulation and movement, and thus, intensive O Vs strength in CWB might viably capture a huge sum of photogenerated e^-, and after that, alter and hinder the interaction of photogenerated e^- and h^+ and generate of more photogenerated h^+ [49,50]. At the same time, the captured e^- at O Vs of $W_{18}O_{49}$ might

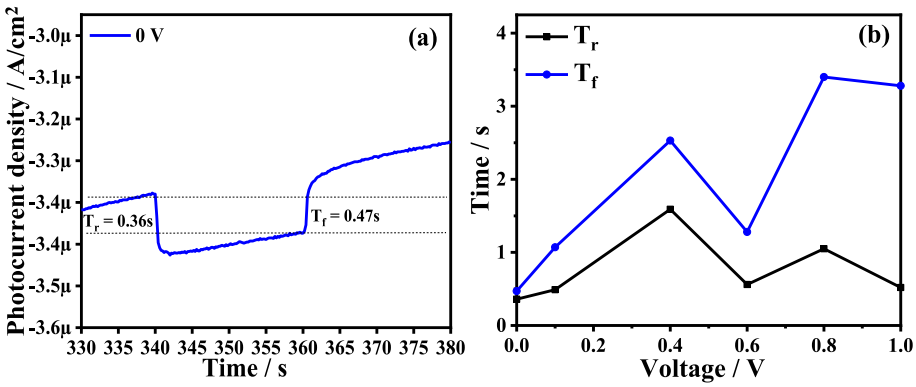

Fig. 9. Photoresponse of CWB-2 based PEC PDs: (a) J-t curve at 0V and (b) Response time (T_r and T_f).

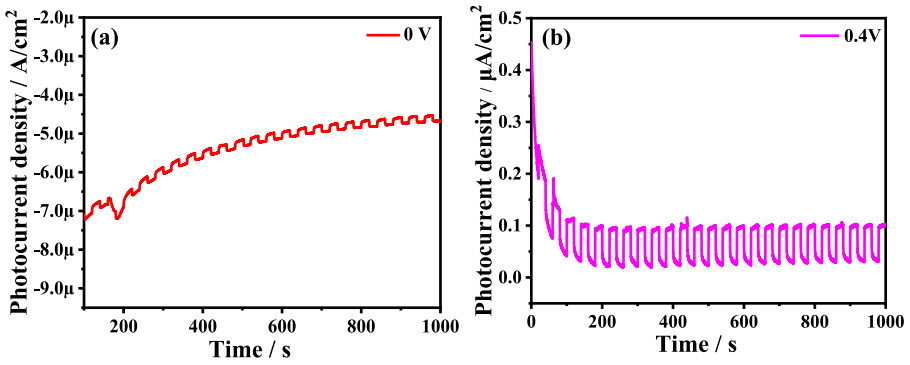

Fig. 10. Photoresponse stability of CWB-2 at 0 V (a) and 0.4 V (b).

interact with available photons to immediately reach high-energy states and generate LSPR hot electrons, which straightforwardly drives oxygen reduction response to create $\cdot O_2^-$ species or hot electrons due to the LSPR impact of $W_{18}O_{49}$ can infuse into CB of BiOBr for creating a more prominent amount of $\cdot O_2^-$ [17]. In this manner, the photocatalytic degradation action is improved in CWB caused by synergistic effects, counting viable electron exchange and partition, upgraded light absorption, and highly concentrated OV generation by Z-scheme development helped by CQD.

Based on CWB's excellent photogenerated carrier characteristics, self-powered photoelectrochemical-type (PEC) photodetectors (PD) based on CWB-2 has been assembled due to its low cost, facile fabrication, power-free capacity, following above photoelectrochemical measurements described in the absence of voltage [45,46]. As explored in Fig. 9a, the photocurrent density of CWB-based PEC PDs at 0 V is ~16 nA/cm^2, which exhibits self-powered photoresponse of 1.6 μA W^{-1} (Responsitivity: J_{ph}/I, where J_{ph} and I are the photocurrent density and light irradiation intensity). Here, cathodic photocurrent appears at 0 V, which means the photocurrent polarity has been changed through controlling applied voltage [51]. When the CWB photocathode contacts the electrolyte, a built-in electric field is generated at the photocathode/electrolyte interface, giving the self-powered capability [45]. Based on previous description, the Z-scheme electron transfer pathway may occurred. Photogenerated carriers (electrons and holes) are generated by irradiation onto CWB photocathode surface. Due to combination of the photogenerated electrons from the CB of $W_{18}O_{49}$ with holes at the VB of BiOBr, and OH^- in electrolyte move to counter electrode, and is chemically oxidized into hydroxyl radicals (OH*) and lose electron; In the interim, an cathodic photocurrent in the circuit is obtained when electrons are transported to the interface of the CWB photocathode/electrolyte, and are spent by OH* to reduce to OH^-, forming a complete circulation [45,51].

Response time and multicycle stability are moreover pivotal pointers for PDs. The rising time (T_r) is characterized as the time when the J_{ph} rises from 10 to 90 % beneath light irradiation, and the decay time (T_f) is the time when J_{ph} decays from 90 to 10 % as the illuminated light turns off [45,46]. The T_r and T_f of CWB-based PEC UV PDs at 0 V are 0.36s and 0.47s, separately (Fig. 9a). Tr and T_f from 0 V to 1 V are calculated from the corronding photocurrent density-time curves by the same strategy sequentially (Fig. S7), as appeared in Fig. 9b. By constrast, T_r is shorter than T_f, and the response time is the fastest in the absence of applied voltage. Fig. 10 presents the multi-cycle stability of self-powered and small bias driven CWB-based PEC UV PDs. For fresh samples, with increasing number of illumination and darkening cycles at 0V and 0.4V, shown in Fig.10(a and b), the *J*ph tends to stabilize and reaches about ~0.16 μA/cm^2 and~0.08 μA/cm^2 with almost circulating 800 s (40 cycles), which show relatively stable photoexcited charge partition. In addition, as indicated in Table 3S, we have compared the photoresponse performance of the photodetector constructed in this work to that of other photodetectors based on Z-scheme heterostructures [52–56] reported in the literature. The photoresponse characteristics of PEC photodetector reported in this work slightly inferior than that in other photodetectors under the same or similar test conditions. However, considering different synthesis methods reported by other groups for synthesizing similar end product, the Z-scheme heterostructures synthesis scheme as reported in this work is simpler and more accessible. Here solvothermal, fluid stage room-temperature response, and ensuing mellow warm treatment preparation, techniques are used successively in which much lower temperature treatment is required in comparison with CVD deposition methods in other reported works. The above test results indicate that the CWB photoactive materials have potential application in PEC photodetectors.

4. Conclusion

Novel Z-scheme heterostructure using a multi-component photon excitation system based on BiOBr/$W_{18}O_{49}$ coupling with CQDs has been successfully constructed through simple solvothermal, precipitation, and thermal treatment methods. By integration of the CQD electronic mediator and $W_{18}O_{49}$ defect effect, optimal CWB sample has displayed improved photocatalytic degradation of 97 % TC removal and surperior photocurrent response compared to WB or $W_{18}O_{49}$ alone, as well as a self-powered photoelectrochemical photoresponse with a responsivity of 1.6 μA W^{-1} and a rising and decay response time of 0.36s/0.47s. The upgraded photoresponse and photocatalytic execution can be ascribed to the synergistic impact of enhanced light absorption induced by CQD and SPR effect, as well as intense oxygen vacancy and compatible Z-scheme heterostructure-induced accelerated division of photo-produced carriers. These discoveries provide a case for the simple synthesis of novel heterojunctions and an assistance design for advancing the partition proficiency of photogenerated electrons and holes.

CRediT authorship contribution statement

Weiwei Tie: Writing – original draft, Resources, Methodology, Funding acquisition, Conceptualization. **Surjya Sarathi Bhattacharyya:** Writing – review & editing. **Tianci Ma:** Investigation, Data curation. **Shuangyi Yuan:** Investigation, Data curation. **Minghan Chen:** Investigation. **Weiwei He:** Resources. **Seung Hee Lee:** Writing – review & editing.

Declaration of competing interest

The authors declare that they have no known competing financial interests or personal relationships that could have appeared to influence the work reported in this paper.

Acknowledgments

This research was supported by the Natural Science Foundation of Henan Province (232300421242), China; the Youth Backbone Teacher Funding Project in Universities of Henan Province (2021GGJS145), China; the innovation and entrepreneurship training Program of Henan Province (202310480029, 202410480012); the Key Scientific Research Project plan in Universities of Henan Province (22A430036), China. SH Lee would like to thank to the support of the National Research Foundation of Korea (NRF) grant funded the Korea government (MSIT) (No. 2019R1A5A8080326).

Appendix A. Supplementary data

Supplementary data to this article can be found online at https://doi.org/10.1016/j.carbon.2024.119707.

References

[1] C. Turro, Fixing photocatalysts, Nat. Chem. 14 (2022) 487–488.
[2] Q. Yao, H. Li, J. Xue, S. Jiang, Q. Zhang, J. Bao, Promoting photocatalytic H_2 evolution through retarded charge trapping and recombination by continuously distributed defects in methylammonium lead iodide perovskite, Angew. Chem. Int. Ed. 62 (2023) e202308140.
[3] J. Di, C. Chen, Y. Wu, Y.X. Zhao, C. Zhu, Y. Zhang, C.D. Wang, H.L. Chen, J. Xiong, M.Z. Xu, J.X. Xia, J.D. Zhou, Y.X. Weng, L. Song, S.Z. Li, W. Jiang, Z. Liu, Polarized Cu–Bi site pairs for non-covalent to covalent interaction tuning toward N_2 photoreduction, Adv. Mater. 34 (2022) 2204959.
[4] M.Z. Ma, Z.A. Huang, D.E. Doronkin, W.J. Fa, Z.Q. Rao, Y.Z. Zou, R. Wang, Y. Q. Zhong, Y.H. Cao, R.Y. Zhang, Ultrahigh surface density of Co-N_2C single-atom-sites for boosting photocatalytic CO_2 reduction to methanol, Appl. Catal. B Environ. 300 (2022) 120695.
[5] M.H. Liu, G.G. Zhang, X.C. Liang, Z.M. Pan, D.D. Zheng, S.B. Wang, Z.Y. Yu, Y. D. Hou, X.C. Wang, Rh/Cr_2O_3 and CoOx cocatalysts for efficient photocatalytic water splitting by poly (triazine imide) crystals, Angew. Chem. Int. Ed. 135 (2023) e202304694.
[6] M.A. Iqbal, S. Akram, S. khalid, B. Lal, S.U. Hassan, R. Ashraf, G. Kezembayeva, M. Mushtaq, N. Chinibayeva, A. Hosseini-Bandegharaei, Advanced photocatalysis as a viable and sustainable wastewater treatment process: a comprehensive review, Environ. Res. 253 (2024) 118947.
[7] Y. Lei, J. Luo, X.G. Yang, T. Cai, R.J. Qi, L.Y. Gu, Z. Zheng, Thermal evaporation of large-area SnS_2 thin films with a UV-to-NIR photoelectric response for flexible photodetector applications, ACS Appl. Mater. Interfaces 12 (2020) 24940–24950.
[8] L.F. Yang, J. Guo, S.Y. Chen, A.Q. Li, J. Tang, N. Guo, J. Yang, Z.Z. Zhang, J. W. Zhou, Tailoring the catalytic sites by regulating photogenerated electron/hole pairs separation spatially for simultaneous selective oxidation of benzyl alcohol and hydrogen evolution, J. Colloid Interface Sci. 659 (2024) 776–787.
[9] J. Di, W. Jiang, Recent progress of low-dimensional metal sulfides photocatalysts for energy and environmental applications, Mater. Today Catal 1 (2023) 100001.
[10] M.Y. Wang, P. Yu, X.S. Liu, J.J. Tian, C.Y. Kang, W.F. Zhang, Tailoring band gaps of $KBiO_3$-$NaBiO_3$ heterostructures by the interface actions for enhancing visible light photoelectric response, J. Alloys Compd. 917 (2022) 165509.
[11] J.M. Wu, J. Du, X.Y. He, X.W. Guo, Preparation of heterojunction catalysts for photocatalysis by in-situ synthesis: what we should do next? ChemCatChem 16 (2024) e202301234.
[12] A.A. Isari, M. Mehregan, S. Mehregan, F. Hayati, R.R. Kalantary, B. Kakavandi, Sono-photocatalytic degradation of tetracycline and pharmaceutical wastewater using WO_3/CNT heterojunction nanocomposite under US and visible light irradiations: a novel hybrid system, J. Hazard Mater. 390 (2020) 122050.
[13] Y. Zhong, X.Y. Zhang, Y.M. Wang, X.T. Zhang, X.M. Wang, Carbon quantum dots from tea enhance z-type BiOBr/C_3N_4 heterojunctions for RhB degradation: catalytic effect, mechanisms, and intermediates, Appl. Surf. Sci. 639 (2023) 158254.
[14] Ref Jiufu Chen, Yang Qi, Junbo Zhong, Jianzhang Li, Clemens Burda, Microwave-assisted preparation of flower-like C_{60}/BiOBr with significantly enhanced visible-light photocatalytic performance, Appl. Surf. Sci. 540 (2021) 148340.
[15] J. Abdul Nasir, A. Munir, N. Ahmad, T. Haq, Z. Khan, Z. Rehman, Photocatalytic Z-scheme overall water splitting: recent advances in theory and experiments, Adv. Mater. 33 (2021) 2105195.
[16] C. Liao, W.H. Jing, F. Wang, Y. Liu, 3D In_2S_3/C/Fe_3C nanofibers for Z-scheme photocatalytic CO_2 conversion to acetate, Mater, Today Catal 3 (2023) 100030.
[17] S.N. Ji, J.T. Dong, M.X. Ji, W.J. Zou, S. Yin, Z.G. Chen, J.X. Xia, Rapid dual-channel electrons transfer via synergistic effect of LSPR effect and build-in electric field in Z-scheme $W_{18}O_{49}$/BiOBr heterojunction for organic pollutants degradation, Inorg. Chem. Commun. 138 (2022) 109283.
[18] N. Ma, C.H. Lu, Y.Q. Liu, T.T. Han, W. Dong, D. Wu, X.L. Xu, Direct Z-scheme heterostructure of vertically oriented SnS_2 nanosheet on $BiVO_4$ nanoflower for self-powered photodetectors and water splitting, Small 20 (2024) 2304839.
[19] G.J. Hai, J.F. Huang, Y.N. Jie, L.Y. Cao, L. Wang, C.L. Fu, T. Xiao, M.F. Niu, L. L. Feng, Unveiling the relationships between (010) facets-orientation growth and photocatalytic activity in $W_{18}O_{49}$ nanowires, J. Alloys Compd. 820 (2020) 153127.
[20] M.L. Duan, C.Y. Hu, H. Li, Y.H. Chen, R.T. Chen, W.B. Gong, Z. Lu, N. Zhang, R. Long, L. Song, Y.J. Xiong, Synergizing inter and intraband transitions in defective tungsten oxide for efficient photocatalytic alcohol dehydration to alkenes, JACS Au 2 (5) (2022) 1160–1168.
[21] J. Di, C. Chen, Y. Wu, H. Chen, J. Xiong, R. Long, S.Z. Li, L. Song, W. Jiang, Z. Liu, Asymmetric electron redistribution in niobic-oxygen vacancy associates to tune noncovalent interaction in CO_2 photoreduction, Adv. Mater. 36 (2024) 2401914.
[22] M. Wang, G.Q. Tan, M.Y. Dang, Y. Wang, B.X. Zhang, H.J. Ren, L. Lv, A. Xia, Dual defects and build-in electric field mediated direct Z-scheme $W_{18}O_{49}$/g-C_3N_{4-x} heterojunction for photocatalytic NO removal and organic pollutant degradation, J. Colloid Interface Sci. 582 (2021) 212–226.
[23] D.S. Qiao, X. Qu, X.Y. Chen, B.J. Sun, W.X. Ding, C.T. Chen, X.H. Peng, D.P. Sun, Rational structural design of graphene oxide/$W_{18}O_{49}$ nanocomposites realizes highly efficient removal of tetracycline in water, Appl. Surf. Sci. 619 (2023) 156630.
[24] W.W. Tie, Z.Y. Du, H.W. Yue, S.S. Bhattacharyya, Z. Zheng, W.W. He, S.H. Lee, Self-assembly of carbon nanotube/graphitic-like flake/BiOBr nanocomposite with 1D/2D/3D heterojunctions for enhanced photocatalytic activity, J. Colloid Interface Sci. 579 (2020) 862–871.
[25] A. Hussain, J.H. Hou, M. Tahir, S.S. Ali, Z.U. Rehman, M. Bilal, T.T. Zhang, Q. Dou, X.Z. Wang, Recent advances in BiOX based photocatalysts to enhanced efficiency for energy and environment applications, Catal. Rev. 66 (2024) 119–173.
[26] X.X. Wei, H.T. Cui, S.Q. Guo, L.F. Zhao, W. Li, Hybrid BiOBr-TiO_2 nanocomposites with high visible lightphotocatalytic activity for water treatment, J. Hazard Mater. 263 (2013) 650–658.
[27] G. Cao, Z.S. Liu, P.Z. Feng, Y.L. Zhao, P.Z. Feng, Y.L. Zhao, J.N. Niu, Concave ultrathin BiOBr nanosheets with the exposed {001} facets: room temperature synthesis and the photocatalytic activity, Matr. Chem. Phys. 199 (2017) 131–137.
[28] J.J. Liu, R. Li, B. Yang, Carbon dots: a new type of carbon-based nanomaterial with wide applications, ACS Cent. Sci. 6 (2020) 2179–2195.
[29] M. Miao, L. Mu, S.M. Cao, Y.H. Yang, X. Feng, Dual-functional CDs@ZIF-8/chitosan luminescent film sensors for simultaneous detection and adsorption of tetracycline, Carbohyd. Polym. 291 (2022) 119587.
[30] G.M. Huang, L.J. Liu, L. Chen, L.F. Gao, J.J. Zhu, H.B. Fu, Unique insights into photocatalytic VOCs oxidation over WO_3/carbon dots nanohybrids assisted by water activation and electron transfer at interfaces, J. Hazard Mater. 423 (2022) 127134.
[31] J. Di, J.X. Xia, M.X. Ji, B. Wang, X.W. Li, Q. Zhang, Z.G. Chen, H.M. Li, Nitrogen-doped carbon quantum dots/BiOBr ultrathin nanosheets: in situ strong coupling and improved molecular oxygen activation ability under visible light irradiation, ACS Sustainable Chem. Eng. 4 (2016) 136–146.

[32] X.B. Sun, W.Y. He, T. Yang, H.D. Ji, W. Liu, J.Y. Lei, Y.D. Liu, Z.Q. Cai, Ternary TiO_2/WO_3/CQDs nanocomposites for enhanced photocatalytic mineralization of aqueous cephalexin: degradation mechanism and toxicity evaluation, Chem. Eng. J. 412 (2021) 128679.
[33] X.Y. Xie, S. Li, K.M. Qi, Z.W. Wang, Photoinduced synthesis of green photocatalyst Fe_3O_4/BiOBr/CQDs derived from corncob biomass for carbamazepine degradation: the role of selectively more CQDs decoration and Z-scheme structure, Chem. Eng. J. 420 (2021) 129705.
[34] L.H. Lin, J. Cao, B.D. Luo, B.Y. Xu, S.F. Chen, Visible-light photocatalytic activity and mechanism of novel AgBr/BiOBr prepared by deposition-precipitation, Chin. Sci. Bull. 57 (2012) 2901–2907.
[35] X.Y. Li, R. Zhao, H.F. Li, J. Jiang, L.H. Ai, X.J. Cao, J.L. Liu, H.J. Zou, Y.Y. Duan, Constructing the multilayer O-g-C_3N_4@$W_{18}O_{49}$ heterostructure for deeply photocatalytic oxidation NO, Sep. Purif. Technol. 307 (2023) 122841.
[36] X.M. Tu, S.L. Luo, G.X. Chen, J.H. Li, One-pot synthesis, characterization, and enhanced photocatalytic activity of a BiOBr-graphene composite, Chem. Eur J. 18 (2012) 14359–14366.
[37] N. Song, H.Q. Fan, H.L. Tian, Reduced graphene oxide/ZnO nanohybrids: Metallic Zn powder induced one-step synthesis for enhanced photocurrent and photocatalytic response, Appl. Surf. Sci. 353 (2015) 580–587.
[38] Xu, X. Bai, L.K. Guo, S.J. Yang, P.K. Jin, L. Yang, Facial fabrication of carbon quantum dots (CDs)-modified N-TiO_{2-x} nanocomposite for the efficient photoreduction of Cr(VI) under visible light, Chem. Eng. J. 357 (2019) 473–486.
[39] J. Chen, X. Xiao, Y. Wang, Z. Ye, Ag nanoparticles decorated WO_3/g-C_3N_4 2D/2D heterostructure with enhanced photocatalytic activity for organic pollutants degradation, Appl. Surf. Sci. 467 (2019) 1000–1010.
[40] C.Y. Pei, Y.G. Chen, L. Wang, W. Chen, G.B. Huang, Step-scheme $WO_3/CdIn_2S_4$ hybrid system with high visible light activity for tetracycline hydrochloride photodegradation, Appl. Surf. Sci. 535 (2021) 147682.
[41] S.H. Ding, P. Tan, N. Meng, X.X. Cao, W. Wang, WO_3/N-CDs photocatalyst with Z-scheme heterojunction for efficient tetracycline degradation under visible and near-infrared light, Colloid. Surfaces A 675 (2023) 132086.
[42] L.B. Jiang, X.Z. Yuan, G.M. Zeng, J. Liang, X.H. Chen, H.B. Yu, H. Wang, Z.B. Wu, J. Zhang, T. Xiong, In-situ synthesis of direct solid-state dual Z-scheme WO_3/g-C_3N_4/Bi_2O_3 photocatalyst for the degradation of refractory pollutant, Appl. Catal. B Environ. 227 (2018) 376–385.
[43] C. Zhao, F. Ran, L. Dai, C. Li, C. Zheng, C. Si, Cellulose-assisted construction of high surface area Z-scheme C-doped g-C_3N_4/WO_3 for improved tetracycline degradation, Carbohydr. Polym. 255 (2021) 117343.
[44] X.Y. Liu, Z. Yang, L. Zhang, In-situ fabrication of 3D hierarchical flower-like β-Bi_2O_3@CoO Z-scheme heterojunction for visible-driven simultaneous degradation of multi-pollutants, J. Hazard Mater. 403 (2021) 123566.
[45] Z.T. Shao, L.H. Qu, M.Q. Cui, J. Yao, F. Gao, W. Feng, H.Q. Lu, Achieving High-performance self-powered visible-blind ultraviolet photodetection using alloy engineering, ACS Appl. Mater. Interf. 15 (2023) 43994–44000.
[46] Y.Q. Liu, C.H. Lu, M.W. Luo, T.T. Han, Y.Q. Ge, W. Dong, X.Y. Xue, Y.X. Zhou, X. L. Xu, Vertically oriented SnS_2 on MoS_2 nanosheets for high-photoresponsivity and fast-response self-powered photoelectrochemical photodetectors, Nanoscale Horiz 7 (2022) 1217–1227.
[47] R.K. Das, J.P. Kar, S. Mohapatra, Enhanced photodegradation of organic pollutants by carbon quantum dot (CQD) deposited Fe_3O_4@mTiO_2 nano-pom-pom balls, Ind. Eng. Chem. Res. 55 (2016) 5902–5910.
[48] H.R. Zuo, C.Y. Wu, H.Y. Du, H. Shi, Y.W. Fu, T.T. Zhang, Q.S. Yan, Construction of Z-scheme Ag-AgBr/$Bi_2O_2CO_3$/CNT heterojunctions with remarkable photocatalytic performance using carbon nanotubes as efficient electronic mediators, Chemosphere 302 (2022) 134927.
[49] C.Y. Chen, T. Jiang, J.H. Hou, et al., Oxygen vacancies induced narrow band gap of BiOCl for efficient visible-light catalytic performance from double radicals, J. Mater. Sci. Technol. 114 (2022) 240–248.
[50] C.Z. Jin, M.Y. Liu, C.Y. Wang, X.A. Yang, L.L. Yao, W.B. Zhang, A ZnO-002/amorphous Bi_2WO_6 heterojunction with enhanced electron-hole separation for high-performance Cr(VI) photoreduction, Appl. Surf. Sci. 648 (2024) 159007.
[51] R. Tan, Y. Qin, M.W. Liu, H.J. Wang, J.L. Li, Z. Luo, L.Y. Hu, W.L. Gu, C.Z. Zhou, Nickel single-atom catalyst-mediated efficient redox cycle enables self-checking photoelectrochemical biosensing with dual photocurrent readouts, ACS Sens. 8 (2023) 263–269.
[52] R.Y. Yu, H. Qiao, Z.Y. Huang, P.H. Tang, X. Qi, In situ synergistic $Ti_2CTx/W_{18}O_{49}$ heterostructure for photoelectrochemical photodetector with improved and durable photoresponse, J. Phys. Chem. C 127 (2023) 21656–21664.
[53] C.H. Lu, M.W. Luo, W. Dong, Y.Q. Ge, T.T. Han, Y.Q. Liu, X.Y. Xue, N. Ma, Y. Y. Huang, Y.X. Zhou, X.L. Xu, $Bi_2Te_3/Bi_2Se_3/Bi_2S_3$ cascade heterostructure for fast-response and high-photoresponsivity photodetector and high-efficiency water splitting with a small bias voltage, Adv. Sci. 10 (2023) 2205460.
[54] P. Chauhan, A.B. Patel, G.K. Solanki, H.K. Machhi, C.K. Sumesh, S.S. Soni, V. Patel, V.M. Pathak, Ultrasonically exfoliated nanocrystal-based Z-Scheme $SnSe_2/WSe_2$ heterojunction for a superior electrochemical photoresponse, J. Phys. Chem. C 125 (2021) 14729–14740.
[55] C.H. Lu, W. Dong, Y.Q. Zou, Z.Y. Wang, J.Y. Tan, X. Bai, N. Ma, Y.Q. Ge, Q.Y. Zhao, X.L. Xu, Direct Z-Scheme $SnSe_2$/SnSe heterostructure passivated by Al_2O_3 for highly stable and sensitive photoelectrochemical photodetectors, ACS Appl. Mater. Interfaces 15 (2023) 6156–6168.
[56] N. Ma, C.H. Lu, Y.Q. Liu, T.T. Han, W. Dong, D. Wu, X.L. Xu, Direct Z-scheme heterostructure of vertically oriented SnS_2 nanosheet on $BiVO_4$ nanoflower for self-powered photodetectors and water splitting, Small 20 (2024) 2304839.